Advanced Composites and Hybrid Materials (2025) 8:401
https://doi.org/10.1007/s42114-025-01483-y

RESEARCH

3D triazine-based covalent organic framework and glass fiber hybrid network for enhanced thermal insulation in polyphenylene sulfide composites

Jaeyeon Kim[1] · Jaekyung Lee[1] · Oju Kwon[1] · Subin Lee[2] · Minsu Kim[1] · Pei-Chen Su[3] · Jooheon Kim[1,2]

Received: 26 June 2025 / Revised: 4 September 2025 / Accepted: 24 September 2025

Abstract
In this study, a polyphenylene sulfide (PPS)-based composite was developed by incorporating triazine-based covalent organic frameworks (TCOFs) and glass fibers (GFs) to simultaneously address the challenges of thermal insulation and flame retardancy in high-temperature environments. The TCOF structure was engineered via an Ostwald ripening process to exhibit a highly porous, partially crystalline architecture, enabling multiscale phonon scattering and effectively hindering thermal transport. In parallel, surface-modified GFs served as a reinforcing scaffold, enhancing mechanical strength and promoting the formation of a robust char layer during combustion. The resulting hybrid composites demonstrated significantly reduced thermal conductivity, reaching as low as 0.056 $W \cdot m^{-1} \cdot K^{-1}$, and outstanding flame retardancy, consistently achieving UL-94 V-0 ratings across all formulations. Morphological analyses confirmed the development of dense, thermally stable char structures in the presence of both fillers. Mechanical testing further revealed that the dual-filler network enhanced the storage modulus and maintained tensile performance, despite the inherent brittleness introduced by the fillers. These findings underscore the synergistic effects of TCOFs and GFs in creating multifunctional PPS composites with superior thermal insulation, flame resistance, and mechanical durability, making them strong candidates for advanced thermal management applications.

Keywords Thermal insulation · Triazine-based covalent organic framework · Polyphenylene sulfide · Glass fiber · Flame retardancy

1 Introduction

Thermal management in high heat-generating environments, such as electronic devices, electric vehicles, and energy storage systems, has become a critical challenge in modern industry [1, 2]. The increasing power density and integration of these systems inevitably lead to excessive heat generation, resulting in thermal accumulation and localized overheating [3, 4]. These thermal issues can degrade system performance, reduce device lifespan, and, in severe cases, pose fire hazards [5]. Consequently, there is a pressing need for thermal insulation materials that offer high thermal resistance, low density, heat resistance, and mechanical stability [6, 7].

Polymer-based composites have gained considerable attention as promising thermal insulation materials due to their processability, design flexibility, and low density—advantages that help mitigate the brittleness and processing challenges associated with conventional inorganic insulation materials [8, 9]. Among available polymers, polyphenylene sulfide (PPS) is widely used across industries as both a structural and insulating material, owing to its excellent heat resistance, chemical resistance, mechanical strength, and dimensional stability. However, despite exhibiting an LOI value of ~ 38% and achieving a UL-94 V-0 rating, which reflect its intrinsic flame resistance, PPS still faces challenges due to its relatively high thermal conductivity (approximately 0.2–0.3 $W \cdot m^{-1} \cdot K^{-1}$) and limited char-forming ability. These factors restrict its effectiveness in

✉ Jooheon Kim
jooheonkim@cau.ac.kr

[1] School of Chemical Engineering, Chung-Ang University, Seoul 06974, Republic of Korea

[2] Department of Intelligent Energy and Industry, Graduate School, Chung-Ang University, Seoul 06974, Republic of Korea

[3] School of Mechanical and Aerospace Engineering, Nanyang Technological University, Singapore, Singapore

Published online: 16 October 2025

high-temperature insulation and flame-retardant systems, particularly under prolonged thermal exposure [10, 11].

To overcome these limitations, a variety of fillers—including inorganic materials (e.g., alumina, silica, boron nitride) and carbon-based additives (e.g., carbon nanotubes, graphene, carbon fibers)—have been incorporated into PPS [12, 13]. Inorganic fillers can enhance flame retardancy and thermal resistance, but their high density and rigid structure often compromise mechanical flexibility and processability [14]. Carbon-based fillers contribute to mechanical reinforcement and thermal stability, but their inherently high thermal conductivity undermines their suitability for thermal insulation [15, 16]. Additionally, achieving uniform dispersion and strong interfacial adhesion often requires complex processing steps [17]. Despite the individual advantages of these fillers, they face structural and functional limitations in simultaneously satisfying the combined requirements of thermal insulation, flame retardancy, and mechanical durability.

In this study, a PPS-based composite was developed by integrating triazine-based covalent organic frameworks (COFs) and glass fibers (GFs), resulting in a material with a continuous three-dimensional porous network, high thermal stability, and excellent mechanical properties. The COFs were synthesized with a grid-like porous architecture via an Ostwald ripening process [18, 19]. This architecture, combined with the continuous fibrous morphology of GF, formed an interconnected, multiphase three-dimensional network within the PPS matrix, comprising both amorphous and crystalline domains. This hybrid network effectively suppressed phonon propagation in amorphous regions and disrupted heat conduction pathways in crystalline regions. The COFs also exhibited a thermal decomposition temperature exceeding 300 °C, enhancing overall thermal stability, while the nitrogen-rich triazine ring structure contributed to improved flame retardancy, achieving UL-94 V-0 certification. Simultaneously, the GF acted as a reinforcing phase, promoting structural integrity and forming a continuous network that enhanced mechanical strength. This synergistic interaction between COFs and GF enabled the development of a robust, continuous three-dimensional porous network, which significantly improved the composite's thermal insulation, flame retardancy, and mechanical performance. These results underscore the potential of the developed composite as a high-performance multifunctional material for thermal insulation and flame-retardant applications under extreme operating conditions.

2 Results and discussion

2.1 Characterization of the fillers

Figure 1 presents a schematic overview of the composite fabrication process. Detailed experimental procedures are available in the Supporting Information.

The morphology of the synthesized triazine-based covalent organic framework (TCOF) and GF, both before and after surface treatment, was analyzed using field-emission scanning electron microscopy (FE–SEM) and transmission electron microscopy (TEM), as shown in Fig. 2. The as-synthesized TCOF (Fig. 2a) exhibited spherical particles with smooth surfaces. After 24 h of aging, the particle surfaces became notably rougher, and internal cavities formed (Fig. 2b), a transformation attributed to dissolution and recrystallization during Ostwald ripening. This

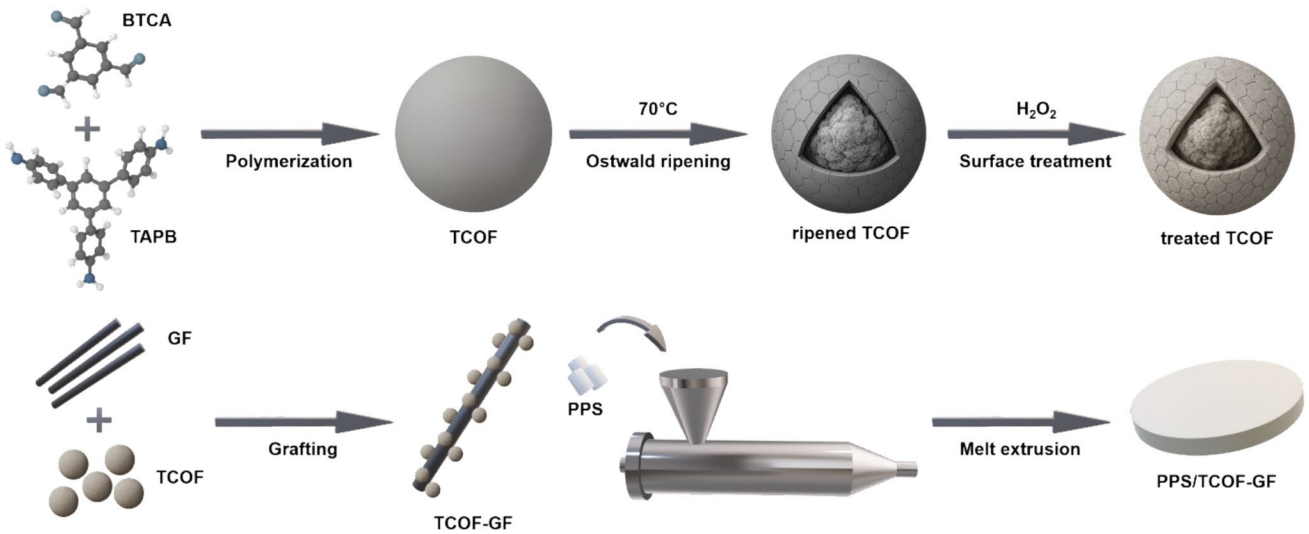

Fig. 1 Schematic illustration of the composite fabrication process

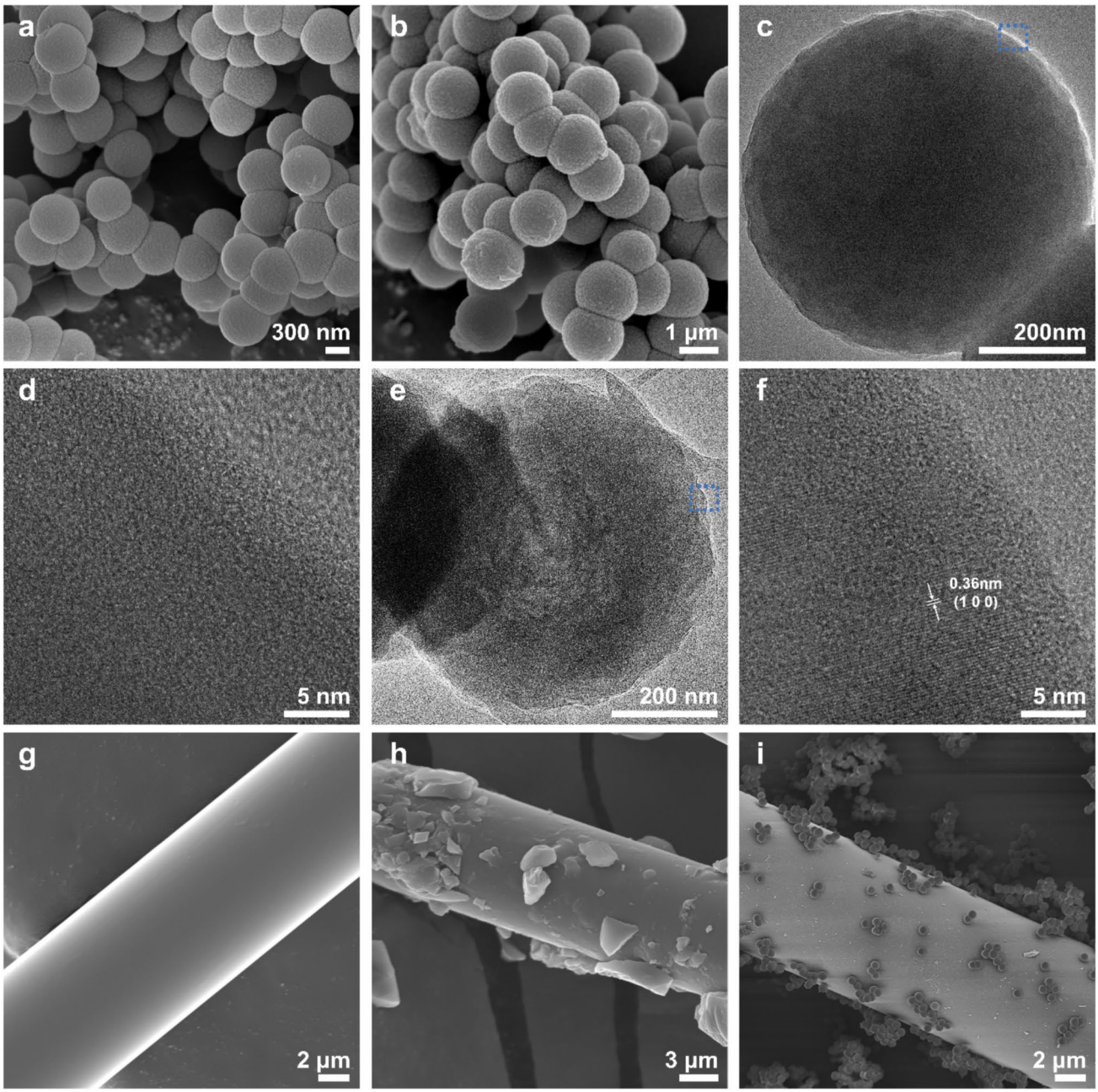

Fig. 2 FE–SEM images of TCOF before (**a**) and after (**b**) Ostwald ripening. TEM and high-resolution TEM images of TCOF before (**c**, **d**) and after (**e**, **f**) ripening. FE–SEM images of pristine GF (**g**), silane-treated GF (**h**), and hybrid filler TCOF-GF (**i**)

structural evolution is driven by the instability of amorphous domains, leading to material reprecipitation along the particle periphery.

TEM analysis revealed that the pristine TCOF (Fig. 2c) possessed a dense, void-free internal structure. Its high-resolution image (Fig. 2d) lacked lattice fringes, indicating a fully amorphous phase. In contrast, the ripened TCOF (Fig. 2e) developed multiple internal voids, and the corresponding high-resolution image (Fig. 2f) showed partially ordered lattice fringes at the particle edges, suggesting localized crystallization. The measured lattice fringe spacing was approximately 0.36 nm, corresponding to the (100) plane of the imine-linked framework, as further supported by diffraction peaks observed in the XRD pattern (Supporting Fig. S1 and Fig. 4a). This confirms the formation of short-range crystalline order in the outer shell during Ostwald ripening.

The formation of the covalent organic framework proceeds through a Schiff-base condensation between

1,3,5-tris(4-aminophenyl)benzene (TAPB) and 2,5-dihydroxyterephthalaldehyde (Dha), yielding extended imine (–C = N–) linkages. FT-IR and solid-state 13 C NMR spectra confirmed the complete consumption of the amine ($–NH_2$) and aldehyde (–CHO) groups, along with the appearance of characteristic imine peaks at ~ 1610 cm^{-1} and 155 ppm, respectively, indicating the successful establishment of the covalent framework. The overall reaction can be represented as:

$$3Ar - NH_2 + 3Ar\prime - CHO \rightarrow COFnetworkwith - C = N - linkages + 3H_2O$$

During synthesis, Ostwald ripening plays a critical role in governing the morphology and crystallinity of the framework. Smaller crystallites gradually dissolve and redeposit onto larger ones, leading to the formation of hollow spherical COFs with mesoporous shells. This recrystallization process not only minimizes surface energy but also enhances long-range order and structural uniformity. The evolution of such mesoporous shells intrinsically impacts the mechanical behavior of the composites. The fusion of nanoscale crystallites reduces structural defects and increases rigidity, facilitating more efficient stress transfer across the filler–matrix interface. Moreover, the hollow mesoporous architecture provides internal free volume and hierarchical porosity that act as stress-dissipating domains, which buffer external loads and suppress crack propagation [20]. Previous studies have further emphasized that interfacial elasticity and stress–relaxation phenomena strongly influence the stabilization of ripening-derived structures, thereby affecting their long-term mechanical stability [21]. Consequently, the combined effects of improved crystallinity and hierarchical morphology endowed by Ostwald ripening contribute significantly to the enhanced rigidity and crack resistance of the composites.

For the GF, the pristine sample (Fig. 2g) displayed a smooth, featureless surface, indicative of the absence of surface functionalization. After silanization (Fig. 2h), the surface roughness increased and nanoscale fragments were observed, confirming the successful grafting of silane coupling agents. The final hybrid filler (Fig. 2i) exhibited uniform anchoring of TCOF particles on the GF surface, validating effective integration via surface treatment.

The elemental composition of both TCOF and silane-treated GF was examined using energy-dispersive X-ray spectroscopy (EDS), as shown in Fig. 3. The TCOF sample (Fig. 3a) exhibited prominent signals of C, O, and N, consistent with the presence of triazine and imine functionalities within the covalent organic framework. The detection of nitrogen further confirms the incorporation of triazine core units into the framework structure. In the case of the GF (Fig. 3b), elemental mapping revealed strong signals of Si and O, as expected for the silicate backbone. Additionally, the presence of sulfur (S) was detected, indicating successful grafting of the 3-(trimethoxysilyl)propyl methacrylate (MPTMS) silane coupling agent, which contains a thiol-derived functional group. These results confirm that the GF surface was chemically modified through silanization.

The structural and thermal properties of the TCOF and GF were analyzed using X-ray diffraction (XRD), Fourier-transform infrared spectroscopy (FT-IR), and thermogravimetric analysis (TGA), as shown in Fig. 4. Figure 4a displays the XRD patterns of TCOF before and after 24 h of Ostwald ripening. The as-synthesized TCOF exhibited a broad background signal with a weak diffraction peak at approximately $2\theta \approx 5.7°$, corresponding to the (100) reflection of the imine-linked COF framework. This is characteristic of a

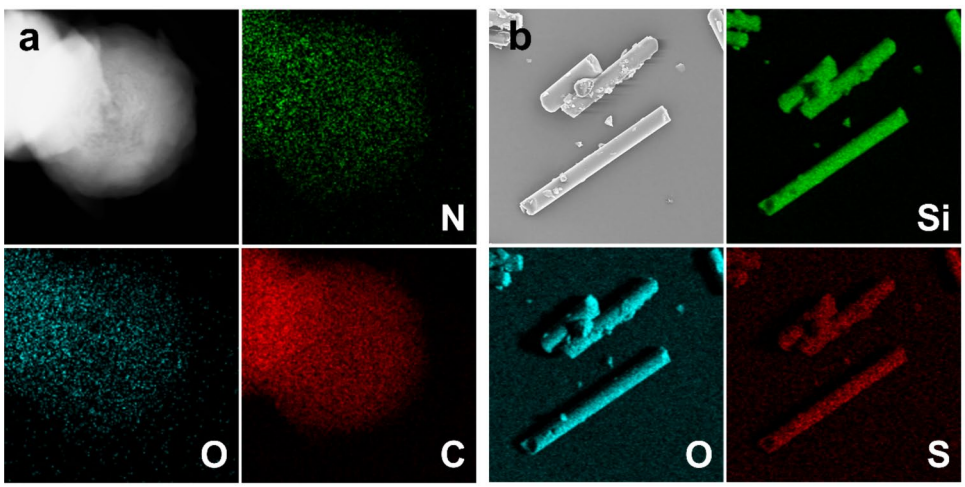

Fig. 3 EDS elemental mappings of a) TCOF and (b) silane-treated GF

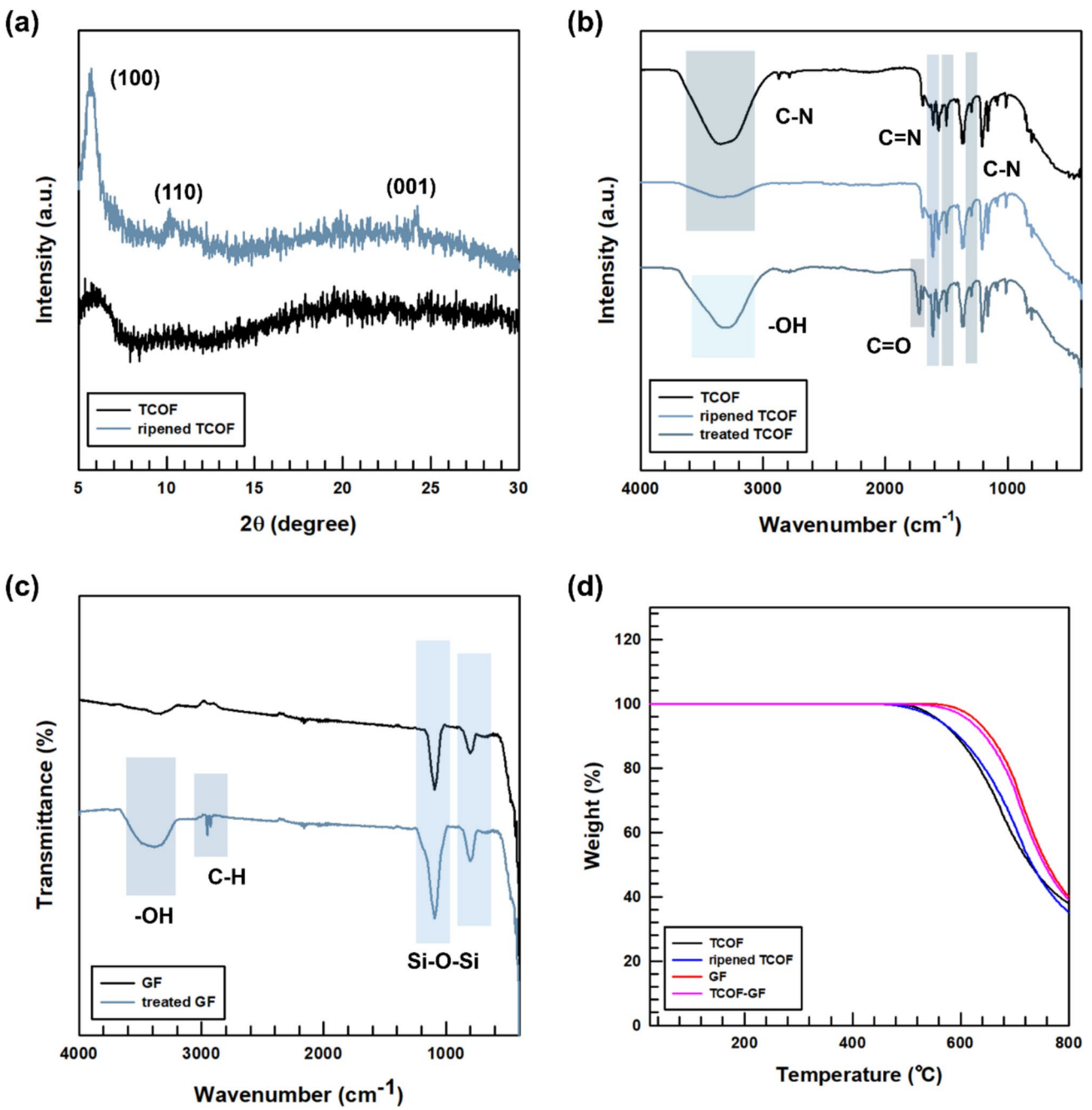

Fig. 4 (**a**) XRD patterns of TCOF before and after 24 h Ostwald ripening. (**b**) FT-IR spectra of TCOF, ripened TCOF, and H_2O_2-treated TCOF. (**c**) FT-IR spectra of GF before and after H_2O_2 treatment. (**d**) TGA curves of TCOF and GF under a nitrogen atmosphere

largely amorphous material with limited ordering. Following Ostwald ripening, an additional peak appeared near 2θ ≈ 9.5°, along with a shoulder around 26°. These features are attributed to partial crystallization and π–π stacking interactions between aromatic domains in the outer shell, indicating that crystallization initiates at the particle surface during ripening [22]. These findings are consistent with the short-range ordering observed in the HRTEM images (Fig. 2f and Supporting Fig. S1). The appearance of sharper diffraction peaks in the ripened TCOF further supports the formation of longer-range crystalline order. This morphological transformation is likely driven by enhanced interfacial stability and reduced Laplace pressure during ripening, which promote mass migration from the particle interior to the shell and lead to progressive cavity formation. Such a mechanism aligns well with previously reported crystallization pathways

in other highly crystalline 3D COF systems undergoing Ostwald ripening [23].

Figure 4b presents FT-IR spectra of pristine TCOF, ripened TCOF, and H_2O_2-treated TCOF. All samples exhibited characteristic vibrational bands at 1609.9 cm^{-1} (C = N stretching), 1500.3 cm^{-1} (C–N stretching), and 1296.3 cm^{-1} (C–N in triazine rings), confirming the presence of imine linkages and triazine units. After Ostwald ripening, a slight increase in the relative intensities of the C = N and C–N bands was observed, suggesting increased framework densification and improved structural ordering [23]. The H_2O_2-treated TCOF showed a new broad absorption band at 3301.9 cm^{-1}, attributed to O–H stretching, indicating the incorporation of hydroxyl groups through surface oxidation. Additionally, a shoulder at 1724.2 cm^{-1} appeared, corresponding to C = O stretching, likely resulting from partial oxidative cleavage during treatment. Figure 4c shows the FT-IR spectra of GF before and after silane modification using MPTMS. Both samples featured characteristic Si–O–Si asymmetric stretching at 1090 cm^{-1} and Si–O–Si symmetric stretching at 802 cm^{-1}. Following silanization, new absorption bands appeared at ~ 2950 and 2924 cm^{-1}, corresponding to C–H stretching from the propyl group in the MPTMS molecule. Simultaneously, the intensity of the broad –OH band near 3380 cm^{-1} increased due to hydrolyzed silanol formation. These spectral changes confirm the successful surface modification of the GF with MPTMS [24].

TGA was conducted under a nitrogen atmosphere to assess the thermal stability of the fillers (Fig. 4d). Both the as-synthesized and ripened TCOF exhibited a single-step thermal degradation beginning at approximately 310 °C, attributed to the decomposition of the imine-linked framework. The onset and profile of thermal degradation were nearly identical between the two, indicating that the introduction of partial crystallinity via ripening had little influence on the overall thermal stability. In contrast, the GF showed minimal weight loss up to 750 °C, consistent with the high thermal resistance of its silicate backbone [25]. The hybrid TCOF–GF displayed a reduced weight loss compared to pristine TCOF, reflecting the contribution of the thermally stable GF component.

Figure 5 presents the FTIR and XRD results of the hybrid TCOF–GF filler. In the FTIR spectrum, the characteristic imine (C = N) stretching of TCOF (~ 1620 cm^{-1}) and the Si–O–Si vibration of GF (~ 1100 cm^{-1}) were both observed, confirming the coexistence of the two components. Importantly, the emergence of a Si–O–C band indicated successful grafting of the COF framework onto the fiber surface. The XRD pattern further supported this hybridization, showing the typical (100) reflection of TCOF at ~ 5.7° alongside the broad amorphous hump of GF centered at ~ 23°. These results collectively verify that the hybrid filler retained the structural features of both TCOF and GF while establishing interfacial bonding between them.

The surface chemical states of TCOF, GF, and their hybrid filler were examined using high-resolution X-ray photoelectron spectroscopy (XPS), as shown in Fig. 6. The C 1 s spectrum of pristine TCOF (Fig. 6a) was deconvoluted into five distinct components at binding energies of 284.01, 284.45, 285.10, 286.17, and 287.63 eV, corresponding to C = C, C–C, C = N, C–N, and C–O bonding environments, respectively. These features are attributed to aromatic and π-conjugated carbon systems, imine linkages, triazine units, and minor oxygen-containing groups such as ethers or residual aldehydes. The N 1 s spectrum of pristine TCOF (Fig. 6b) showed three components at 398.34, 399.17, and 400.07 eV, attributed to pyridinic nitrogen (C = N), triazine-type nitrogen, and C–N groups, respectively. The dominant peak at 399.17 eV confirms the structural integrity of the triazine framework. After H_2O_2 treatment, both the C 1 s (Fig. 6c) and N 1 s (Fig. 6d) spectra displayed subtle changes. The C–O peak at 287.63 eV became slightly

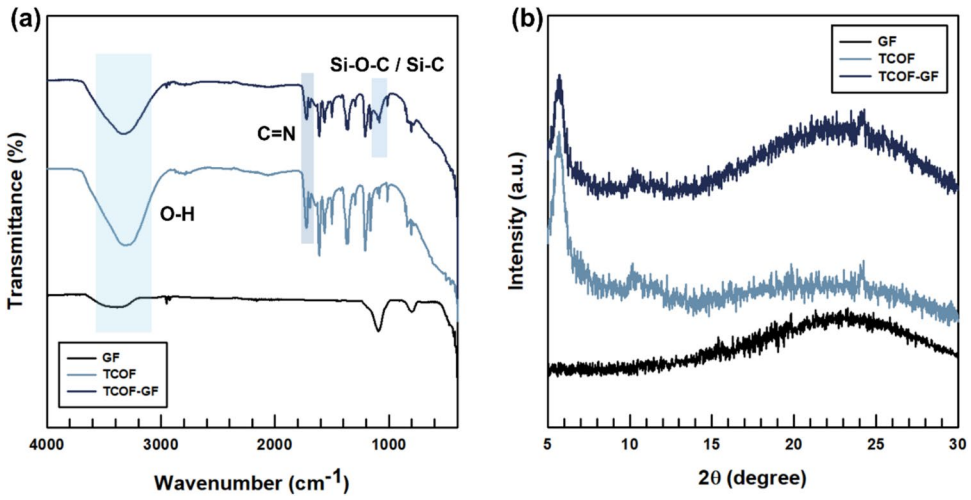

Fig. 5 FTIR spectra and XRD patterns of hybrid TCOF–GF filler

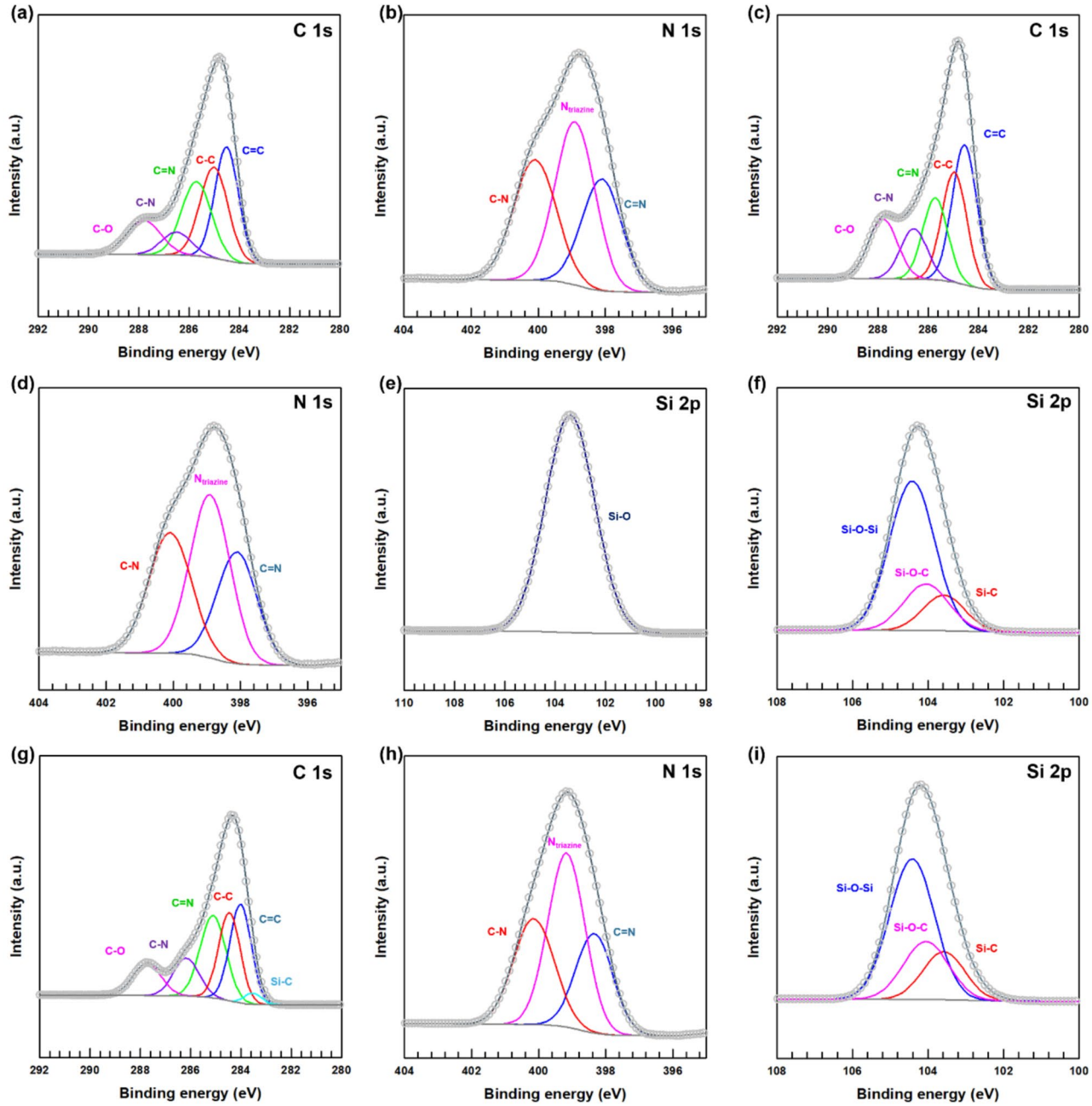

Fig. 6 High-resolution XPS spectra of TCOF, GF, and TCOF–GF hybrid fillers: (**a**) C 1 s spectrum of pristine TCOF, (**b**) N 1 s spectrum of pristine TCOF, (**c**) C 1 s spectrum of F–TCOF, (**d**) N 1 s spectrum of F–TCOF, (**e**) Si 2p spectrum of GF, (**f**) Si 2p spectrum of silane-treated GF, (**g**) C 1 s spectrum of TCOF–GF hybrid, (**h**) N 1 s spectrum of TCOF–GF hybrid, (**i**) Si 2p spectrum of TCOF–GF hybrid

more prominent, and the C–N contribution at 400.07 eV increased modestly, indicating mild surface oxidation and minor protonation of terminal nitrogen atoms. Nevertheless, the overall peak positions and distributions remained largely unchanged, demonstrating that the conjugated COF framework and triazine structure were retained despite surface-level functionalization.

For GF, the Si 2p spectrum of the untreated sample (Fig. 6e) showed a single peak at 103.42 eV, corresponding to Si–O–Si bonding within the silicate network. After MPTMS treatment (Fig. 6f), the peak position remained essentially unchanged, indicating that the underlying silicate framework was intact. However, slight peak broadening was observed, likely due to the formation of Si–O–C and

Si–C bonds from the organosilane, with new components emerging at 102.58 eV (Si–C) and 103.05 eV (Si–O–C). The XPS survey scan (Fig. S2, Supporting Information) further confirmed MPTMS grafting on GF, showing the presence of S and Si signals with corresponding atomic% values. Complementary O 1 s spectra are provided in the Supporting Information (Fig. S3), which corroborate these observations.

In the case of the TCOF–GF hybrid filler, the C 1 s spectrum (Fig. 6g) exhibited contributions from both TCOF- and silane-related species, including C = C, C–C, C = N, C–N, C–O, and an additional Si–C component at 283.6 eV, confirming chemical linkage between the organic framework and silane-modified GF. The N 1 s spectrum (Fig. 6h) retained the characteristic signals of pyridinic nitrogen, triazine nitrogen, and C–N groups, indicating preservation of the TCOF framework on the hybrid surface. Meanwhile, the Si 2p spectrum (Fig. 6i) showed Si–O–Si as the dominant feature, along with contributions from Si–O–C and Si–C, where the relative intensities changed compared with pure GF, providing evidence of interfacial coupling between TCOF and GF.

Figure 7 presents nitrogen adsorption–desorption isotherms and BJH (Barrett–Joyner–Halenda) pore size distribution curves for TCOF before and after the Ostwald ripening process. The isotherm of as-synthesized TCOF (Fig. 6a, black line) displayed a typical Type I profile, indicative of a predominantly microporous structure with limited nitrogen uptake at high relative pressures. The corresponding Brunauer–Emmett–Teller (BET) surface area and total pore volume were measured to be 359.5 m^2/g and 0.190 cm^3/g, respectively, consistent with the compact morphology observed in TEM images (Fig. 2c). These results confirm that the pristine TCOF had a dense structure with restricted accessible porosity.

In contrast, the ripened TCOF (Fig. 6a, red line) exhibited significantly enhanced nitrogen adsorption, along with a well-defined H3-type hysteresis loop, which is characteristic of slit-shaped mesopores formed between agglomerated particles or interparticle voids. The BET surface area increased dramatically to 1067.2 m^2/g, while the total pore volume reached 0.839cm^3/g, signifying a substantial improvement in internal porosity. This dramatic transformation is attributed to Ostwald ripening, where less stable, amorphous regions dissolve and reprecipitate at the outer shell [26]. This process results in the formation of hollow interiors and porous shells while maintaining the particle framework. Evidence of this transformation is visible in TEM images (Fig. 2e), which show the formation of voids, as well as in the emergence of crystalline fringes (Fig. 2f and Fig. S1).

The BJH pore size distribution analysis (Fig. 7b) further confirmed the development of hierarchical porosity. While the as-synthesized TCOF exhibited negligible mesopore contribution, the ripened TCOF demonstrated a broad distribution of mesopores ranging from 4 to 20 nm. This hierarchical pore architecture is particularly beneficial for thermal insulation applications, as it enhances phonon scattering,

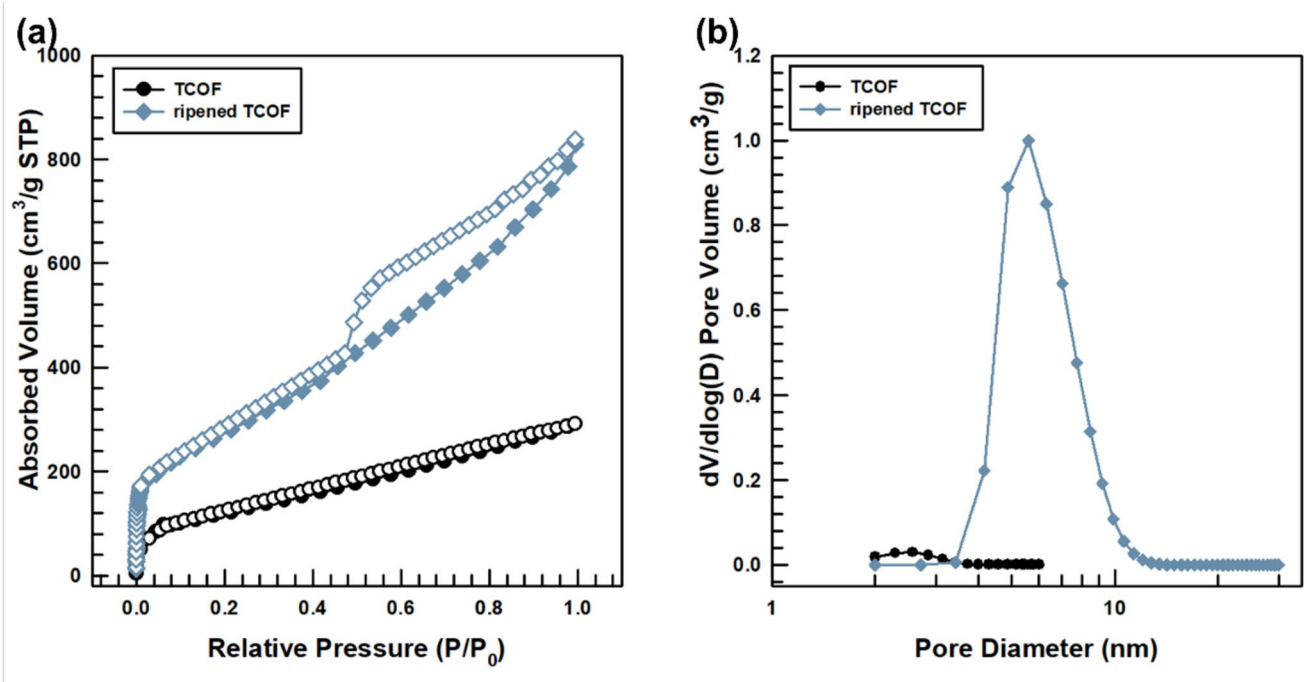

Fig. 7 (**a**) Nitrogen adsorption–desorption isotherms and (**b**) BJH pore size distribution curves of TCOF before and after the Ostwald ripening process

reduces thermal bridging, and suppresses heat transfer [27]. The mesopores (4–20 nm) observed in ripened TCOF (Fig. 6b) are consistent with the Knudsen regime, where pore-wall collisions dominate transport in the 2–50 nm range [28]. In contrast, micropores (< 2 nm) are strongly affected by adsorption phenomena and thus contribute minimally to phonon scattering, in agreement with reports that ultra micropores primarily act as adsorption sites while larger pores produce stronger scattering signals [29]. Therefore, the mesopores, rather than micropores, play the dominant role in suppressing thermal conductivity via Knudsen scattering, as illustrated in Fig. 9. Therefore, the observed porosity evolution not only improves structural accessibility but also enhances the thermal insulating performance of TCOF as a filler material.

2.2 Cross-sectional morphologies of composites

The fracture surface morphologies of PPS composites were examined by FE-SEM to investigate microstructural evolution and filler–matrix interactions (Fig. 8a–i). The neat PPS matrix (Fig. 8a) exhibited a relatively smooth and featureless fracture surface, indicative of limited energy dissipation and inherent brittleness.

With the addition of 1 and 3 wt% of ripened TCOF (Fig. 8b and 8c), the fracture surfaces became notably rougher and displayed crack deflection features. These changes suggest enhanced toughness, likely due to the reinforcing effect of the hierarchical porous TCOF filler. At a higher loading of 5 wt% TCOF (Fig. 8d), the fracture morphology became even more irregular, characterized by tortuous crack paths and the presence of voids. This suggests a disruption of crack propagation and increased interfacial contact area, both contributing to improved energy dissipation. The PPS/GF30 composite (Fig. 8e) exhibited clear evidence of fiber pull-out, indicating that although silane treatment improved the chemical affinity between the fiber and matrix, complete interfacial bonding was not achieved. This indicates an improvement in chemical affinity between the fiber and matrix, although complete interfacial bonding was not achieved.

Notably, the dual-filler composites containing both TCOF and GF (Fig. 8f–h) exhibited more compact and integrated fracture surfaces, with fewer interfacial voids and reduced

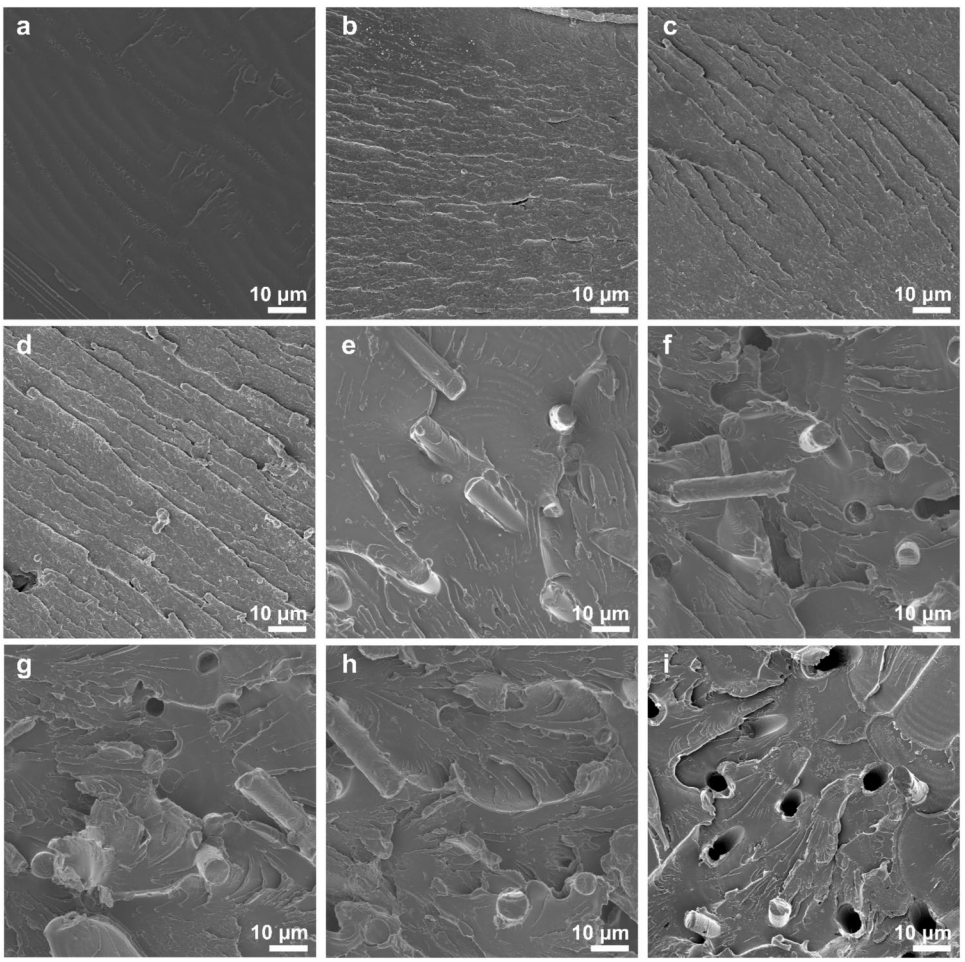

Fig. 8 SEM images of fracture surfaces of (**a**) PPS, (**b**) PPS/TCOF1, (**c**) PPS/TCOF3, (**d**) PPS/TCOF5, (**e**) PPS/GF30, (**f**) PPS/TCOF1–GF30, (**g**) PPS/TCOF3–GF30, (**h**) PPS/TCOF5–GF30, and (**i**) PPS/TCOF5–GF30 (non-ripened). All GFs were surface-treated with silane

fiber pull-out compared to the single-filler systems. These observations reflect improved filler dispersion and stronger interfacial adhesion, indicating a synergistic interaction between the nanostructured TCOF and silane-treated GFs. Among these, the PPS/TCOF5–GF30 composite (Fig. 8h) displayed the most continuous and densely packed morphology, consistent with enhanced mechanical integrity. In contrast, the composite incorporating non-ripened TCOF (Fig. 8i) exhibited fragmented filler domains and weak matrix adhesion. This highlights the critical role of the Ostwald ripening process in developing effective filler–matrix interfaces and achieving the desired composite performance. As a control, a simple physical mixture of PPS/COF and GF was also examined, which showed no distinct interfacial interactions compared to the hybrid filler system (Fig. S12).

2.3 Thermal properties of the composites

The thermal conductivity of PPS composites containing 1, 3, and 5 wt% TCOF was evaluated to assess how porous filler content influences heat transfer (Fig. 9a). The compositions and corresponding thermal conductivity values of the PPS composites are summarized in Table 1. Unless otherwise noted, all TCOF samples underwent 24 h of Ostwald ripening. Neat PPS exhibited a thermal conductivity of 0.211 $W \cdot m^{-1} \cdot K^{-1}$, which progressively decreased to 0.162, 0.141, and 0.119 $W \cdot m^{-1} \cdot K^{-1}$ with increasing TCOF content. This substantial reduction is primarily attributed to the hierarchical porosity developed during ripening. The ripened TCOF features a high specific surface area (1067.2 m^2/g), large pore volume (0.839cm3/g), and broad pore size distribution (4–20 nm), all of which contribute to multiscale phonon scattering. In particular, mesoporous regions promote the Knudsen effect, wherein the phonon mean free path becomes comparable to pore dimensions, thus significantly suppressing thermal conduction. Additionally, π–π stacking and localized surface crystallization within TCOF enhance phonon reflection and interface mismatch, enabling an efficient multidimensional phonon scattering network.

To explore the synergistic effects of nanostructured TCOF and GF, the TCOF content was varied from 1 to 5 wt% while maintaining GF at a constant 30 wt% (Fig. 9b). The PPS/GF30 composite alone showed a thermal conductivity of 0.154 $W \cdot m^{-1} \cdot K^{-1}$, which further decreased to 0.112, 0.071, and 0.056 $W \cdot m^{-1} \cdot K^{-1}$ upon the addition of 1, 3, and 5 wt% TCOF, respectively. This trend indicates enhanced phonon scattering enabled by the dual-filler architecture. By contrast, the PPS/TCOF5–GF30 composite containing non-ripened TCOF displayed a significantly higher thermal conductivity of 0.085 $W \cdot m^{-1} \cdot K^{-1}$, confirming the critical role of Ostwald ripening in generating an effective porous shell for phonon suppression.

TGA was conducted to evaluate thermal decomposition behavior (Fig. 9c). Neat PPS began to degrade around 520 °C, while PPS/TCOF5 and PPS/GF30 both exhibited slightly delayed onset of degradation. Notably, PPS/TCOF5–GF30 showed the highest thermal stability, with the decomposition temperature further shifted to a higher range and enhanced char yield. This trend is attributed to the thermally robust imine and triazine structures in the TCOF framework and the inorganic stability of GF, indicating the synergistic contribution of both fillers. These findings confirm that the incorporation of structurally stable, ripened TCOF and GF not only enhances thermal insulation but also improves high-temperature durability by forming a more resilient composite network.

The Agari–Uno model was applied to analyze the thermal conductivity of PPS composites (Fig. 9d, Table S1). In this model, C1 reflects the ease of forming continuous filler networks, whereas C2 represents phonon scattering at interfaces [30]. For PPS/TCOF–GF, the increased C1 indicates that the hybridization of porous TCOF and fibrous GF promotes a more effective conductive network, consistent with recent reports on filler dispersion and network formation in composites [31]. Furthermore, the relatively low C2 value (0.67) quantitatively reflects enhanced phonon scattering, which arises from the porous–crystalline duality of TCOF (mesoporous core and partially crystalline shell, Fig. 10). This structural duality, in combination with the anisotropic geometry of GF, synergistically intensifies phonon scattering and accounts for the observed reduction in thermal conductivity of the hybrid composites. As detailed in the Supporting Information, the calculated model exhibited close agreement with experimental values, reaffirming the trend of thermal conductivity reduction with increasing TCOF content. Notably, the extracted parameter C2 was significantly low, indicating that the TCOF domains did not form continuous thermally conductive networks but rather acted as effective phonon-scattering barriers.

In the TCOF–GF hybrid system, the model fitting revealed an even steeper decline in thermal conductivity, associated with a further reduction in the C2 value. Despite the intrinsic thermal conductivity of GF, the presence of TCOF disrupted potential conductive pathways and intensified phonon scattering at heterogeneous interfaces. These results underscore a synergistic effect arising from the dual-filler architecture, wherein interfacial mismatch and hierarchical structuring collectively contribute to enhanced thermal insulation.

To complement the Agari–Uno analysis, the Hamilton–Crosser model was further applied with shape factors of $n = 3$ for TCOF and $n = 6$ for GF, together with a correction factor (η_s) to account for interfacial resistance and pore-induced scattering. As summarized in Table S3 and illustrated in Figure S6 (Supporting Information), the corrected

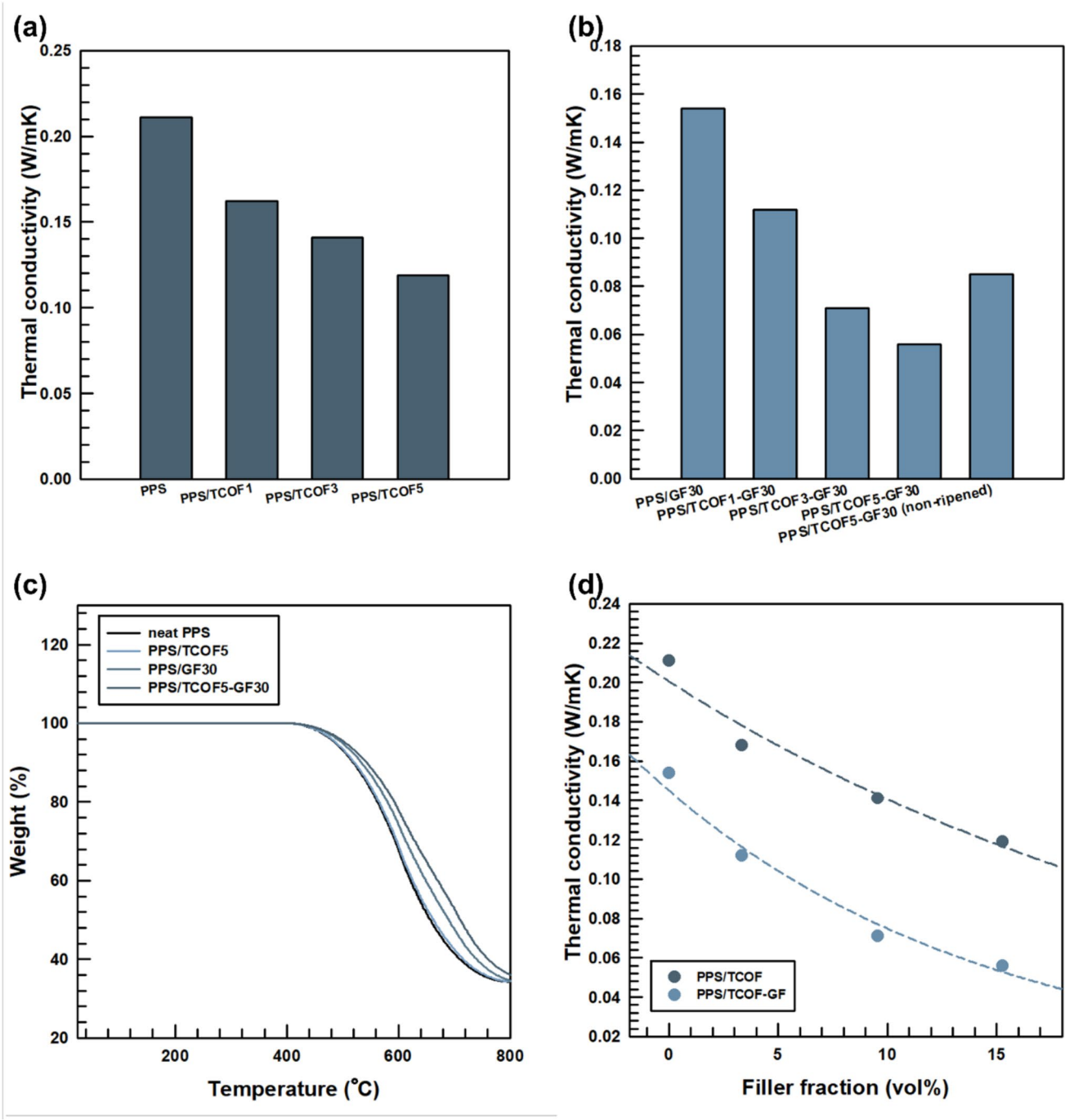

Fig. 9 (**a**) Thermal conductivity of PPS composites containing 1–5 wt% ripened TCOF. (**b**) Thermal conductivity of dual-filler systems (TCOF-GF30), including non-ripened TCOF. ((**c**) TGA of selected PPS composite samples. (**d**) Thermal conductivity predictions using the Agari–Uno model

predictions show improved agreement with experimental data, while the remaining deviation highlights multiscale phonon scattering in the hierarchical TCOF–GF networks.

Figure 10 schematically illustrates the synthesis pathway and structural evolution of TCOF and its hybridization with glass fiber (GF) for thermal insulation applications. The polymerization of BTCA and TAPB yields uniform amorphous TCOF spheres, which undergo a crystallization-driven Ostwald ripening process at 70 °C. During this process, imine exchange dynamics promote surface-oriented crystallization, while the inner amorphous core gradually dissolves, resulting in a hierarchical structure comprising a crystalline

Table 1 Composition and thermal conductivity of PPS composites

Category	Sample	TCOF (wt%)	GF (wt%)	Thermal conductivity ($W\ m^{-1}\cdot K^{-1}$)
Neat matrix	PPS	0	0	0.211
Single-filler	PPS/TCOF1	1	0	0.162
	PPS/TCOF3	3	0	0.141
	PPS/TCOF5	5	0	0.119
	PPS/GF30	0	30	0.154
Hybrid	PPS/TCOF1-GF30	1	30	0.069
	PPS/TCOF3-GF30	3	30	0.063
	PPS/TCOF5-GF30	5	30	0.059
	PPS/TCOF5-GF30 (non-ripened)	5	30	0.092

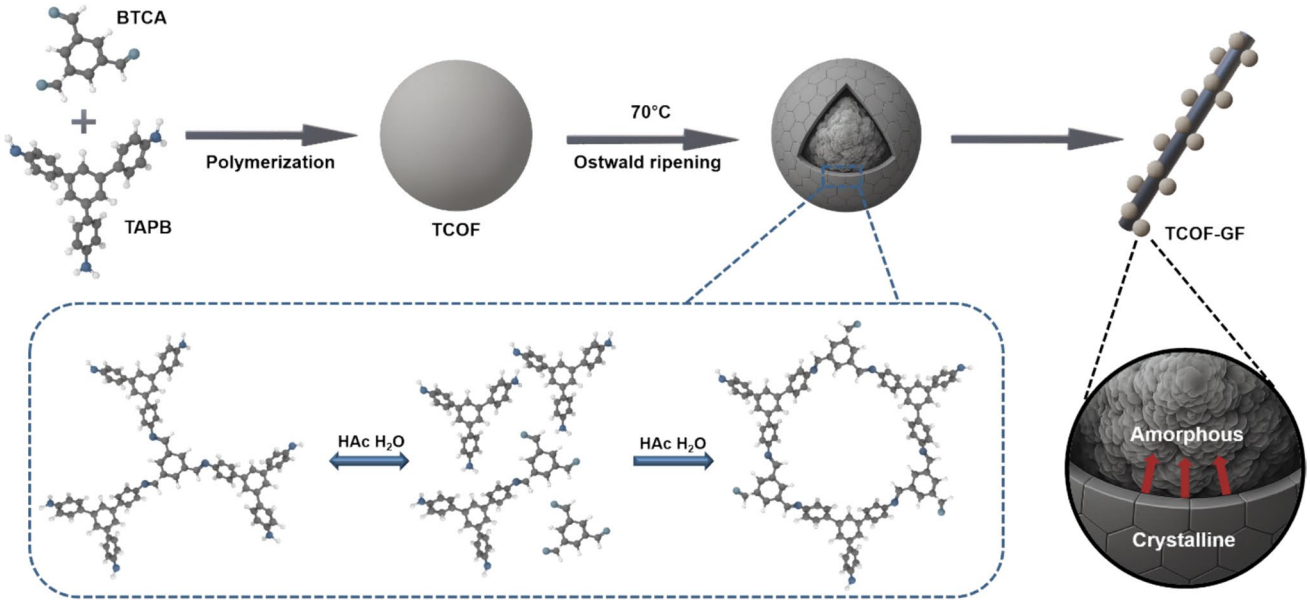

Fig. 10 Schematic illustration of the thermal insulation mechanism in the PPS composite

outer shell and an amorphous porous interior [32]. This anisotropic transformation is critical for thermal insulation, as the outer crystalline domains induce phonon reflection, while the internal mesoporosity facilitates extensive phonon scattering through the Knudsen effect [33]. Subsequent grafting onto silane-treated GF enables the formation of a hybrid filler (TCOF–GF), where TCOF domains are heterogeneously anchored along the GF surface. This architecture combines the rigidity and dispersion benefits of GF with the multidimensional phonon-scattering capability of the TCOF shell, leading to synergistically enhanced thermal insulation performance in polymer composites Figure 11.

As shown in Fig. 12(a), neat PPS exhibits two sharp heat release rate (HRR) peaks with the highest intensity, reflecting rapid and uncontrolled volatile release during decomposition. The incorporation of TCOF or GF leads to a noticeable decrease in peak HRR, and the hybrid PPS/TCOF5–GF30 displays the most pronounced suppression, confirming its superior capability to mitigate heat release. A similar trend is observed in the cumulative total heat release (THR, Fig. 12b), where the hybrid composite records the lowest total value, indicating a significant reduction in combustible fuel generation. Smoke evolution is also influenced by the fillers; the total smoke production (TSP) profiles in Fig. 12(c) demonstrate that PPS/TCOF5–GF30 produces the least smoke, consistent with the reduced release of aromatic and sulfur-containing volatiles identified in the TG–FTIR analysis. Furthermore, the mass retention curves (Fig. 12d) reveal that the hybrid retains the largest char fraction, signifying the formation of a dense and stable carbonaceous layer. This compact char effectively impedes heat and oxygen transfer, while the nitrogenous volatiles (NH_3, HNCO)

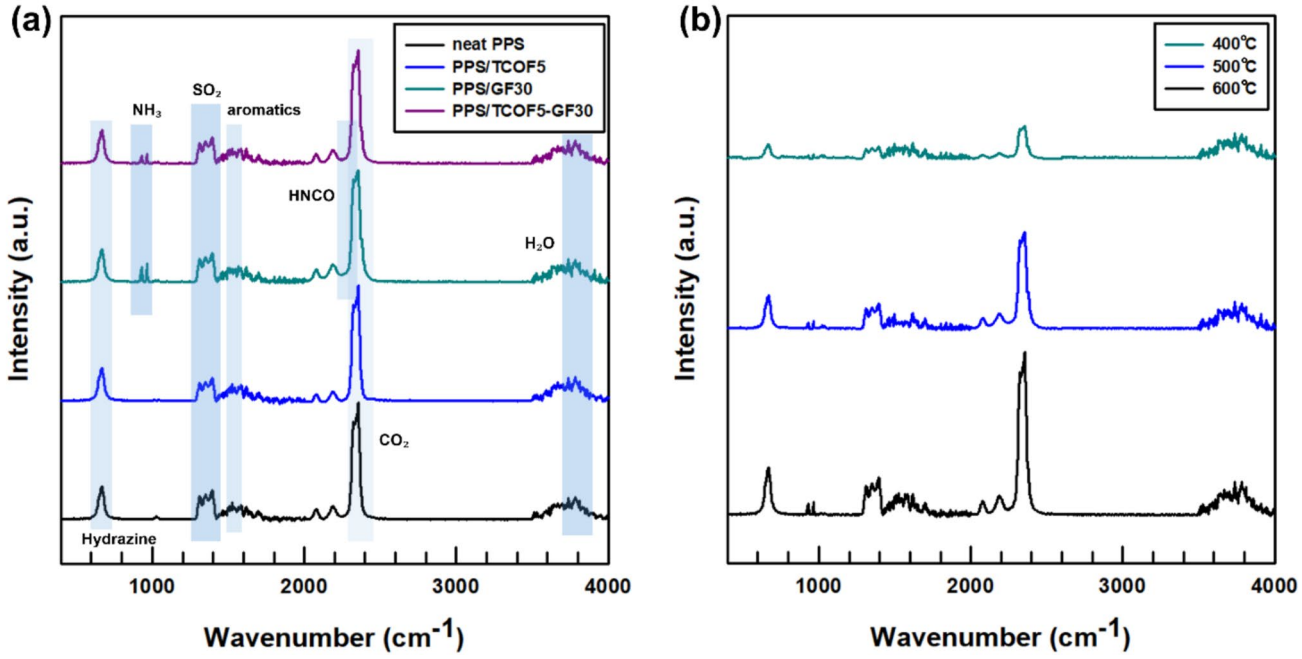

Fig. 11 (**a**) shows the FTIR spectra of the evolved gases from neat PPS and the composites. Neat PPS exhibits typical degradation features of sulfur-containing aromatic polymers, including H_2O (≈3736 cm^{-1}), CO_2 (2360, 2344, 2310, and 670 cm^{-1}), carbonyl-containing volatiles (≈1794 cm^{-1}), SO_2 (1361 and 1151 cm^{-1}), H_2S (2615–2550 cm^{-1}), and aromatic fragments near 1510 cm^{-1}. With the incorporation of TCOF, additional nitrogenous species such as NH_3 (930–965 cm^{-1}), a broad hydrazine-related band (≈950–1000 cm^{-1}), and HNCO (≈2270 cm^{-1}) appear, suggesting a gas-phase flame-retardant action from the triazine framework. PPS/GF30 shows a similar volatile profile to neat PPS but with reduced intensities and delayed maxima, consistent with the barrier effect of the fiber network. The hybrid PPS/TCOF5–GF30 combines both features: nitrogenous volatiles are evident, while the sulfur- and carbonyl-related bands are attenuated and shifted to higher temperatures, confirming a synergistic mechanism of gas-phase dilution and condensed-phase blocking, (**b**) provides the temperature-resolved FTIR spectra of PPS/TCOF5–GF30, which highlight the sequential release of different gaseous species during decomposition. At lower temperatures, H_2O and CO_2 dominate the spectrum, while with increasing temperature, the emergence of NH_3 and HNCO bands indicates the decomposition of the triazine framework. At the same time, the intensity of SO_2 and H_2S bands is significantly reduced and their evolution shifted to higher temperature compared with neat PPS, reflecting suppression of sulfurous volatiles by the hybrid structure. This temperature-resolved analysis demonstrates that the hybrid composite not only delays the onset of decomposition but also alters the volatile composition toward nitrogenous species, thereby reducing the fuel contribution of sulfurous gases and providing an additional gas-phase inhibition pathway.

detected in TG–FTIR act in the gas phase to dilute flammable species and quench radicals. The combination of condensed-phase barrier action and gas-phase inhibition explains the synergistic flame-retardant performance of PPS/TCOF–GF composites, manifested as reduced HRR, lower THR, suppressed smoke release, and enhanced char yield.

Vertical UL-94 flame tests were conducted to evaluate the flame retardancy of PPS composites. As shown in Fig. S8 and summarized in Table 2, all tested composites—including neat PPS and filler-loaded variants—achieved a UL-94 V-0 rating, with limiting oxygen index (LOI) values up to 41.3%. Post-burning images (Fig. S8b) revealed that the char layers formed in composites containing TCOF and GF were more compact and continuous than those of neat PPS, suggesting enhanced thermal shielding.

The superior flame retardancy observed can be attributed to the characteristics of the incorporated fillers. TCOF, enriched with nitrogen-containing triazine rings, enhances flame resistance by releasing inert gases during decomposition and promoting the formation of a stable, insulating char layer. Its imine-linked framework contributes additional thermal stability, delaying degradation—a trend corroborated by the TGA results (Fig. 9d) [34, 35].

GF acts as a physical scaffold that reinforces the char layer and helps maintain the composite's structural integrity during combustion. The combination of TCOF and GF in hybrid systems establishes a hierarchical filler architecture that enhances barrier formation by effectively obstructing both heat and oxygen penetration into the material. This layered protection contributes significantly to thermal shielding and flame suppression [36].

Overall, the outstanding flame-retardant performance of the PPS/TCOF–GF composites arises not only from the intrinsic flame resistance of PPS but also from the synergistic interplay between the nitrogen-rich, char-promoting TCOF and the thermally stable, reinforcing GF. These

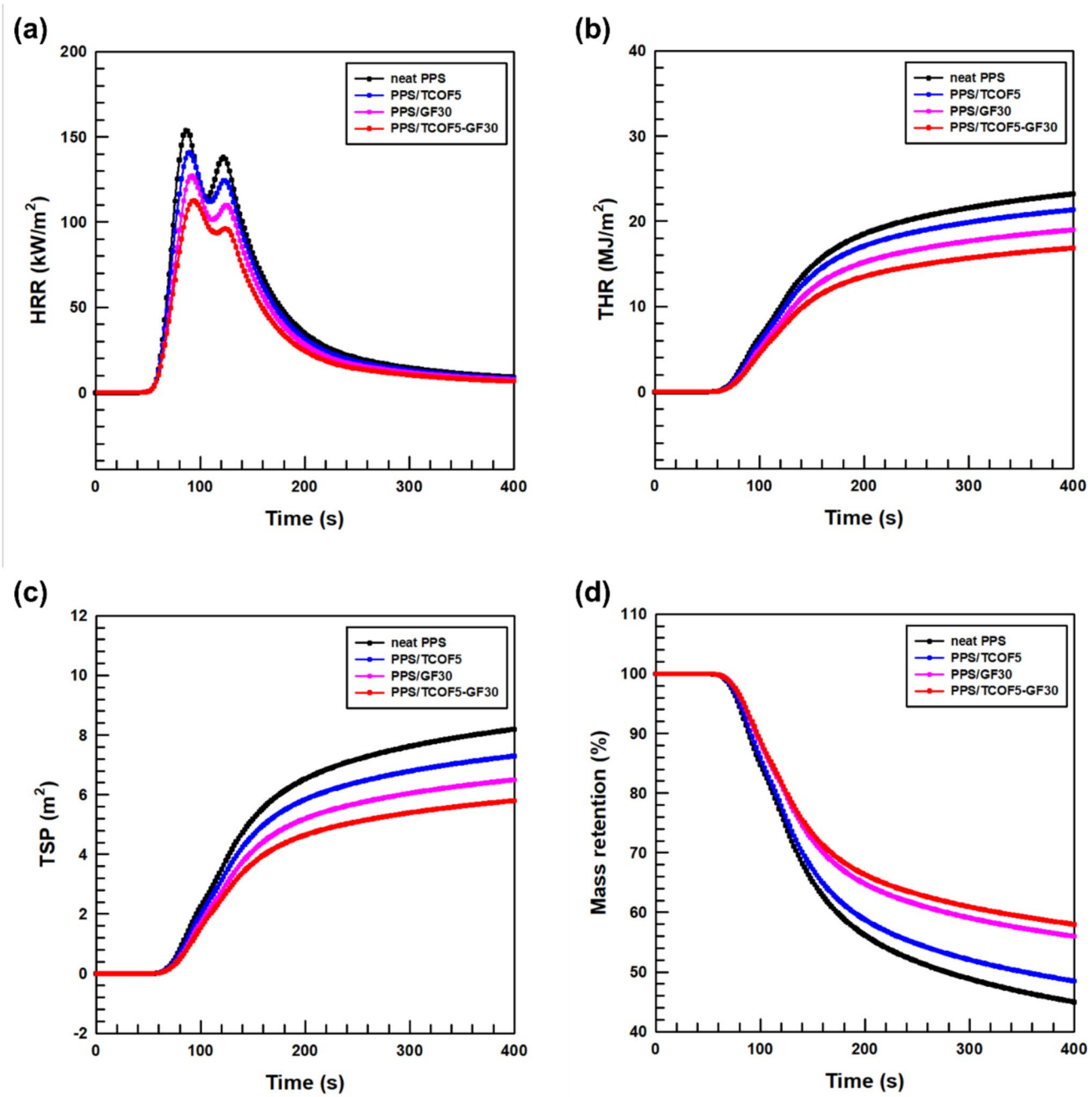

Fig. 12 Cone calorimeter results of PPS and its composites: (**a**) HRR, (**b**) THR, (**c**) av-HRR, and (**d**) TSP

Table 2 UL-94 rating and LOI values of PPS-based composites

Sample	UL-94 Rating	LOI (%)
Neat PPS	V-0	38.2 ± 0.1
PPS/TCOF5	V-0	40.5 ± 0.1
PPS/GF30	V-0	39.7 ± 0.2
PPS/TCOF5–GF30	V-0	41.3 ± 0.1

findings underscore that strategically engineered filler combinations can further elevate the flame resistance of already flame-retardant polymer matrices without resorting to halogenated additives.

To further investigate the flame-retardant mechanisms, SEM analysis was performed on the post-combustion char residues (Fig. S9). Neat PPS (Fig. S9a) exhibited a severely fragmented and porous char morphology with widespread

microcracking and structural collapse, indicating insufficient thermal stability and weak char-forming capability. In contrast, the PPS/TCOF5 sample (Fig. S9b) formed a relatively continuous and dense char structure, with interconnected carbonaceous domains and reduced crack propagation. This is attributed to the thermal decomposition of TCOF, which generates stable aromatic and nitrogen-containing fragments that promote char formation and enhance structural retention.

The PPS/GF30 composite (Fig. S9c) retained a fibrous framework in the residue, where the glass fibers are clearly visible and embedded within the char layer. These fibers act as a thermally stable skeleton, although partial delamination and local voids suggest limited matrix-fiber bonding during combustion. Remarkably, the PPS/TCOF5–GF30 hybrid composite (Fig. S9d) displayed the most cohesive and compact char layer, with minimal porosity and a sponge-like cellular structure, indicating effective reinforcement of the carbonaceous network. This morphology supports the synergistic interaction between TCOF and GF, where TCOF promotes stable char formation and GF maintains physical integrity, jointly contributing to enhanced flame retardancy.

2.4 Mechanical properties of composites

The mechanical performance of the composite films was assessed through tensile testing, as shown in Fig. 13. Figure 13a illustrates the tensile behavior of neat PPS and composites incorporating various amounts of TCOF. Neat PPS exhibited a tensile strength of 58.6 MPa and an elongation at break of 2.37%, consistent with its inherently brittle nature. Upon incorporating 1–5 wt% TCOF, a progressive decrease in tensile strength was observed, reaching 50.9 MPa at 5 wt%. This reduction is attributed to weak filler–matrix interfacial bonding and stress concentrations arising from the rigid and porous nature of the TCOF particles [37]. Similarly, the elongation at break decreased with higher TCOF content, suggesting that the porous filler limited polymer chain mobility and flexibility within the matrix.

Figure 13c presents the stress–strain behavior of composites reinforced with 30 wt% GF, with and without TCOF. The PPS/GF30 composite showed a marked improvement in tensile strength, increasing to 84.9 MPa, primarily due to the high stiffness and load-bearing capacity of the aligned GFs. However, this enhancement came at the cost of reduced ductility, with elongation at break falling to 1.50%. The incorporation of 5 wt% TCOF into the GF-reinforced system (PPS/TCOF5–GF30) led to a slight decrease in tensile strength to 76.7 MPa.

The addition of GF countered the brittleness induced by TCOF. In the hybrid system, PPS/TCOF5–GF30 exhibited a tensile strength of 76.7 MPa, slightly lower than PPS/GF30 (84.9 MPa). This modest reduction can be attributed to partial coverage of the GF surface by the rigid, porous TCOF particles, which may reduce the effective PPS–GF contact area and introduce localized stress concentrations despite silanization. Similar effects have been observed in nanofiller-modified systems, where enhanced reinforcement was often accompanied by minor changes in adhesion [38]. Taken together, these results imply that while minor interfacial disturbances may occur, the overall adhesion is largely preserved and the multifunctional benefits (thermal insulation and flame retardancy) justify this trade-off. High-magnification SEM images of the GF–TCOF–PPS interfaces (Fig. S4) further confirm the enhanced filler–matrix adhesion and reduced interfacial voids.

Dynamic mechanical analysis (DMA, Fig. S11) revealed that the hybrid composites exhibited an increased storage modulus compared with neat PPS, confirming the reinforcing contribution of the dual-filler network. In addition, the tan δ peak shifted slightly toward higher temperatures, suggesting restricted chain mobility due to improved interfacial interactions. Although the incorporation of TCOF led to a moderate reduction in tensile strength compared with PPS/GF30, the hybrid composites maintained balanced mechanical performance with enhanced stiffness and interfacial compatibility.

3 Conclusion

A novel PPS composite system was successfully developed through the co-integration of hierarchically porous triazine-based COFs and silane-treated GFs. The TCOFs, synthesized via Ostwald ripening, featured a mesoporous core and a partially crystalline outer shell, facilitating effective phonon scattering. As a result, the thermal conductivity was reduced from 0.211 $W \cdot m^{-1} \cdot K^{-1}$ (neat PPS) to 0.056 $W \cdot m^{-1} \cdot K^{-1}$ in the PPS/TCOF5–GF30 hybrid composite. Concurrently, the incorporation of GF enhanced the tensile strength from 58.6 MPa (neat PPS) to 84.9 MPa in PPS/GF30. Although the hybrid PPS/TCOF5–GF30 composite exhibited a slightly lower tensile strength of 76.7 MPa, it maintained comparable elongation at break, reflecting a well-balanced mechanical performance. The resulting composites also demonstrated outstanding flame-retardant properties, achieving UL-94 V-0 ratings and an LOI value up to 41.3%. Notably, the hybrid composites formed dense, crack-resistant char layers, providing an effective barrier during thermal degradation. Overall, the dual-filler strategy significantly improved thermal insulation, flame retardancy, and preserved robust mechanical properties of the PPS matrix without the use of halogenated flame retardants. These findings demonstrate a promising pathway for designing high-performance polymer composites tailored for thermally demanding and safety–critical applications.

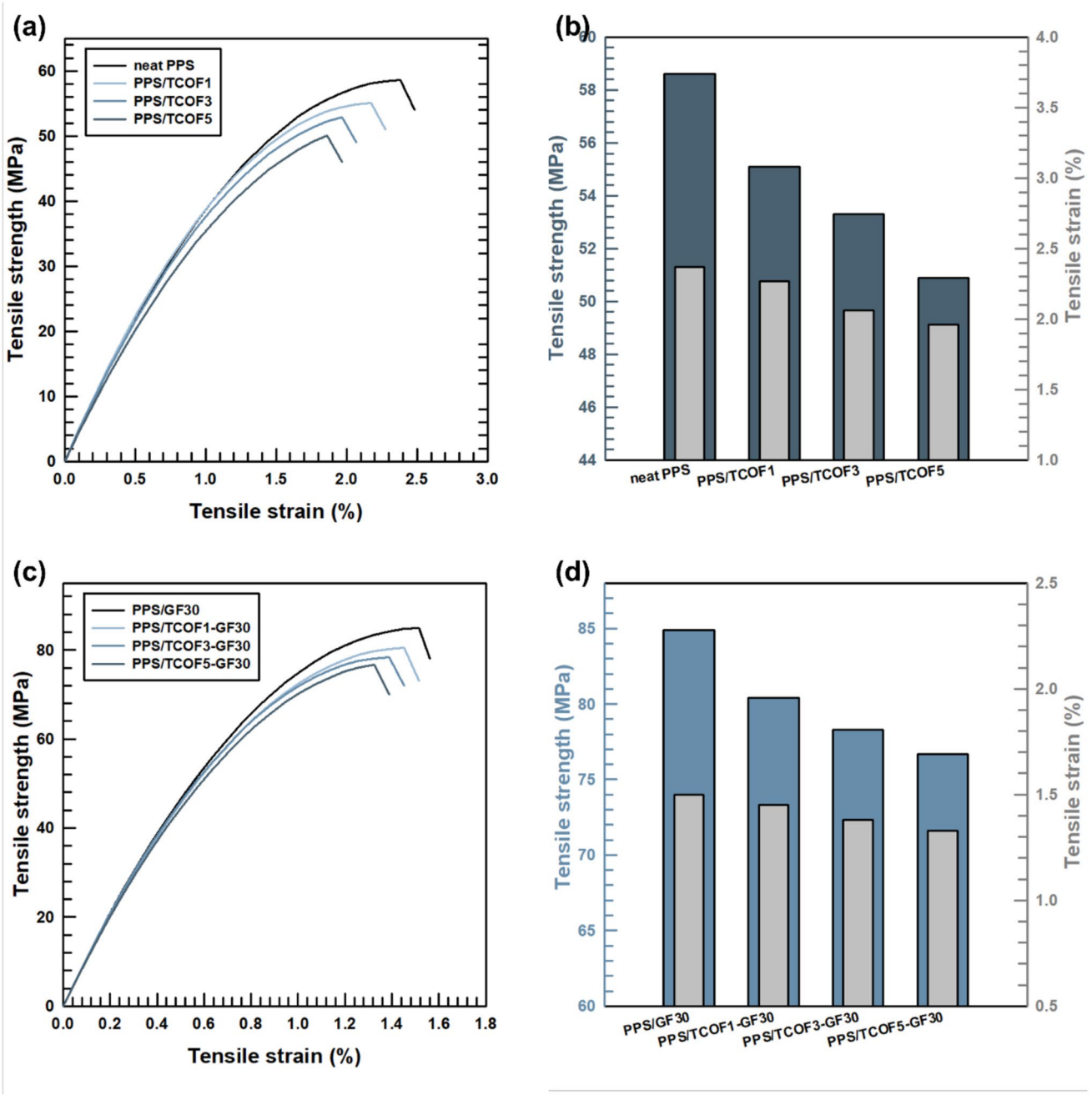

Fig. 13 (**a**) Tensile stress–strain curves of neat PPS and PPS composites containing 1–5 wt% TCOF. (**b**) Tensile strength and elongation at break of PPS/TCOF composites. (**c**) Tensile stress–strain curves of GF30-reinforced composites with and without TCOF. (**d**) Tensile strength and elongation at break of PPS/TCOF–GF30 hybrid composites

Supplementary Information The online version contains supplementary material available at https://doi.org/10.1007/s42114-025-01483-y.

Author contributions Jaeyeon Kim: Conceptualization, Methodology, Investigation, Data curation, Formal analysis, Writing – original draft, Writing- Reviewing and Editing. Jaekyung Lee: Data curation, Formal analysis. Oju Kwon: Data curation, Formal analysis. Subin Lee: Data curation, Formal analysis. Minsu Kim: Investigation, Formal analysis. Pei-Chen Su: Supervision, Project administration. Jooheon Kim: Supervision, Project administration, Funding acquisition.

Funding This work was supported by the National Research Foundation of Korea (NRF) grant funded by the Korea government (MSIT) (RS-2022-NR068145) and supported by the Korea Institute of Energy Technology Evaluation and Planning(KETEP) grant, funded by the Korean government (MOTIE) (RS-2024-00398346, ESS Big

Data-Based O&M and Asset Management Technical Manpower Training).

Data availability No datasets were generated or analysed during the current study.

Declarations

Competing interests The authors declare no competing interests.

References

1. Braconnier DJ, Toth EZ, Martinez JA et al (2025) Exceptional thermal conductivity in printed dielectrics through compositional and microstructural design. Adv Mater. https://doi.org/10.1002/adma.202418984
2. Cao C, Ji S, Jiang Y et al (2024) Mitigating the overheat of stretchable electronic devices via high-enthalpy thermal dissipation of hydrogel encapsulation. Adv Mater. https://doi.org/10.1002/adma.202401875
3. Sun K, Zhang B, Gao K et al (2024) Localized temperature engineering enables writing of heterostructures in glass for polarized photoluminescence of perovskites. ACS Nano 18:6550–6557. https://doi.org/10.1021/acsnano.3c12356
4. Nam D, Lee G, Kim J (2023) Effect of phosphorus vacancies on activity of Fe-doped Nickel phosphide by NaBH4 reduction for efficient oxygen evolution under alkaline conditions. J Ind Eng Chem 123:201–208. https://doi.org/10.1016/j.jiec.2023.03.035
5. Longchamps RS, Yang XG, Wang CY (2022) Fundamental insights into battery thermal management and safety. ACS Energy Lett 7:1103–1111. https://doi.org/10.1021/acsenergylett.2c00077
6. Dong H, Wei S, Chen W et al (2025) Bioinspired lignocellulose foam: exceptional toughness and thermal insulation. ACS Nano. https://doi.org/10.1021/acsnano.4c11945
7. Meng T, Zhu L, Kriney H et al (2025) Hierarchical biogenic-based thermal insulation foam. ACS Nano 19:911–919. https://doi.org/10.1021/acsnano.4c12328
8. Wang J, Liu L, Dong W et al (2024) Ultra-high radial elastic aerogel fibers for thermal insulation textile. Adv Funct Mater. https://doi.org/10.1002/adfm.202417873
9. Zhang X, Zhou J, Wu K et al (2024) Simultaneous enhancement of thermal insulation and impact resistance in transparent bulk composites. Adv Mater. https://doi.org/10.1002/adma.202311817
10. Cai W, You J, Wang W et al (2024) Double-hindered phenolic SiO2 composites with excellent oxidation resistance and thermal stability for enhanced thermal oxidation stability of PPS. Chem Eng J. https://doi.org/10.1016/j.cej.2024.150662
11. Fu MC, Ueda M, Ando S, Higashihara T (2020) Development of novel triazine-based poly(phenylene sulfide)s with high refractive index and low birefringence. ACS Omega 5:5134–5141. https://doi.org/10.1021/acsomega.9b04152
12. Zhu S, Li M, Yang Y et al (2025) Effect of molecular weight of water-based sizing agents on CF processability and CF/PPS composite performance. Chem Eng J. https://doi.org/10.1016/j.cej.2025.164645
13. Kim J, Heo SJ, Lee D et al (2024) Highly strong carbon fibers through synergistic carbonization process of sulfonated poly(p-phenylene sulfide) and carbon nanotube. Carbon. https://doi.org/10.1016/j.carbon.2024.118814
14. Rohart V, Laberge Lebel L, Dubé M (2020) Improved adhesion between stainless steel heating element and PPS polymer in resistance welding of thermoplastic composites. Compos Part B Eng. https://doi.org/10.1016/j.compositesb.2020.107876
15. Yang L, Sun M, Huang G et al (2024) Construction of PPS based carbon fiber photothermal foam for crude oil absorption and seawater desalination. Chem Eng J. https://doi.org/10.1016/j.cej.2024.153180
16. Wang H, Huo S, Chevali V et al (2025) Carbon fiber reinforced thermoplastics: from materials to manufacturing and applications. Adv Mater. https://doi.org/10.1002/adma.202418709
17. Tian S, Zhang Y, Sha Q et al (2024) PPS/TA-PEI/β-FeOOH membranes with powerful photo-Fenton self-cleaning capability for efficient oil–water emulsion separation. Chem Eng J. https://doi.org/10.1016/j.cej.2024.150069
18. Kandambeth S, Venkatesh V, Shinde DB et al (2015) Self-templated chemically stable hollow spherical covalent organic framework. Nat Commun. https://doi.org/10.1038/ncomms7786
19. Liu YY, Li XC, Wang S et al (2020) Self-templated synthesis of uniform hollow spheres based on highly conjugated three-dimensional covalent organic frameworks. Nat Commun. https://doi.org/10.1038/s41467-020-18844-4
20. Meinders MBJ, Van Vliet T (2004) The role of interfacial rheological properties on Ostwald ripening in emulsions. Adv Colloid Interface Sci 108:119–126. https://doi.org/10.1016/j.cis.2003.10.005
21. Liu Y, Yang Y, Sun Y et al (2019) Ostwald ripening-mediated grafting of metal-organic frameworks on a single colloidal nanocrystal to form uniform and controllable MXF. J Am Chem Soc 141:7407–7413. https://doi.org/10.1021/jacs.9b01563
22. Liu B, Zhao L, Liu Y et al (2025) Triazine-containing covalent organic polymer-derived grid-like multilocular spheres for aqueous supercapacitors. Adv Mater. https://doi.org/10.1002/adma.202419124
23. Xiong Z, Sun B, Zou H et al (2022) Amorphous-to-crystalline transformation: general synthesis of hollow structured covalent organic frameworks with high crystallinity. J Am Chem Soc 144:6583–6593. https://doi.org/10.1021/jacs.2c02089
24. Kuttner C, Tebbe M, Schlaad H et al (2012) Photochemical synthesis of polymeric fiber coatings and their embedding in matrix material: Morphology and nanomechanical properties at the fiber-matrix interface. ACS Appl Mater Interfaces 4:3484–3492
25. Afshari M, Dinari M (2021) A novel triazine-based covalent organic framework: enhancement fire resistance and mechanical performances of thermoplastic polyurethanes. Compos Part A Appl Sci Manuf. https://doi.org/10.1016/j.compositesa.2021.106453
26. Li H, Liu J, Wang Y et al (2025) Hollow covalent organic framework (COF) nanoreactors for sustainable photo/electrochemical catalysis. Coord Chem Rev. https://doi.org/10.1016/j.ccr.2024.216240
27. Deng Z, Wang L, Peng B et al (2025) Optimization of electromagnetic wave absorption properties by formation of magnetoelectric synergistic effect of COF-derived carbon composite Fe/Fe3C. Chem Eng J. https://doi.org/10.1016/j.cej.2025.159457

28. Krishna R (2016) Investigating the validity of the Knudsen diffusivity prescription for mesoporous and macroporous materials. Ind Eng Chem Res 55:4749–4759. https://doi.org/10.1021/acs.iecr.6b00762
29. Zou Y, Shi Z, Shi J et al (2024) "Honeycomb-like" triazine-based covalent organic framework derivative for remarkably improving both flame retardancy and mechanical properties of epoxy resin. Constr Build Mater 426. https://doi.org/10.1016/j.conbuildmat.2024.136166
30. Agari Y, Uno T (1986) Estimation on thermal conductivities of filled polymers. J Appl Polym Sci 32:5705–5712. https://doi.org/10.1002/app.1986.070320702
31. He F, Wang Y, Zheng W et al (2022) Effective thermal conductivity model of aerogel thermal insulation composite. Int J Therm Sci. https://doi.org/10.1016/j.ijthermalsci.2022.107654
32. Doremus JG, Lotsi B, Sharma A, McGrier PL (2024) Photocatalytic applications of covalent organic frameworks: synthesis, characterization, and utility. Nanoscale. https://doi.org/10.1039/D4NR03204G
33. Zhang Y, Tian Y, Xu N et al (2024) In situ mechanical foaming of hierarchical porous MoC for assembling ultra-light, self-cleaning, heat-insulation, flame-retardant, and infrared-stealth device. Adv Funct Mater. https://doi.org/10.1002/adfm.202414910
34. Tang W, Qian L, Chen Y et al (2019) Intumescent flame retardant behavior of charring agents with different aggregation of piperazine/triazine groups in polypropylene. Polym Degrad Stab. https://doi.org/10.1016/j.polymdegradstab.2019.108982
35. Fan Z, Tang J, Zhang W et al (2025) Processable and recyclable covalent organic framework gel electrolytes. Adv Mater. https://doi.org/10.1002/adma.202501223
36. Chen J, Wang J, Ding A et al (2019) Flame retardancy and mechanical properties of glass fibre reinforced polyethylene composites filled with novel intumescent flame retardant. Compos Part B Eng. https://doi.org/10.1016/j.compositesb.2019.107555
37. Burtch NC, Heinen J, Bennett TD et al (2018) Mechanical properties in metal–organic frameworks: emerging opportunities and challenges for device functionality and technological applications. Adv Mater. https://doi.org/10.1002/adma.201704124
38. Kim S, Lee SH, Choi S et al (2021) Overcoming the trade-off relationship between mechanical and adhesive properties of acrylic pressure sensitive adhesive thin-film by reinforcing polydopamine-coated silica nanoparticles. Polymer. https://doi.org/10.1016/j.polymer.2021.123937